APEM journal
Advances in Production Engineering & Management
Volume 20 | Number 3 | September 2025 | pp 325–339
https://doi.org/10.14743/apem2025.3.543
ISSN 1854-6250
Journal home: apem-journal.org
Original scientific paper

Optimizing abrasive water jet milling of alumina ceramics with RBF neural networks

Feng, Y.T.[a,*], **Shi, Z.R.**[a], **Yang, X.**[a], **Huang, W.**[a], **Luo, X.**[a], **Li, Y.H.**[a], **Yu, L.**[a]

[a]Geely University of China, Chengdu, P.R. China

ABSTRACT

Abrasive water jet technology is an advanced machining method that combines high-pressure water jet with solid abrasives. Owing to its unique cold-processing characteristics, high flexibility, and environmental bebefits, it has been widely applied in aerospace, medical devices, microelectronics, defense and other fields. Focusing on alumina ceramic plates, this study systematically investigates abrasive water jet (AWJ) milling through an integrated experimental and modeling approach. The research framework consists of three main phases: the development of an experimental design for abrasive water jet milling of alumina ceramics; systematic parameter optimization using single-factor and orthogonal array experiments, with material removal rate and milling depth as key performance indicators; and the application of a radial basis function (RBF) neural network model for milling depth prediction. The experimental results demonstrate that optimal parameter combinations improve machining efficiency by 38 % compared to baseline conditions. The developed RBF model achieves exceptional predictive accuracy, with maximum absolute and relative errors of 0.30 mm and 18.8 %, respectively, and a mean absolute error of 12.01 % across validation trials. This work provides a theoretical foundation for precision machining of advanced ceramics while demonstrating a viable pathway toward intelligent process optimization in AWJ technology.

ARTICLE INFO

Keywords:
Abrasive water jet (AWJ);
Milling;
Alumina ceramic;
Precision machining;
Material removal rate;
Single-factor experiment;
Orthogonal array;
RBF neural network

**Corresponding author:*
fengyetao917@163.com
(Feng, Y.T.)

Article history:
Received 16 June 2025
Revised 30 August 2025
Accepted 3 September 2025

1. Introduction

Abrasive Water jet (AWJ) technology is an advanced machining method that integrates high-pressure water jet with solid abrasives. Owing to its unique cold-processing characteristics, high flexibility, and environmental benefits, it has been widely adopted in aerospace, medical devices, microelectronics, and defense industries. As industrial materials evolve toward high hardness, high-temperature resistance, and brittleness, the limitations of conventional pure water jet technology have become increasingly apparent—such as the reliance on ultra-high pressure for machining hard materials (leading to prohibitive equipment costs) and low processing efficiency. By introducing abrasive particles into high-velocity water jets, AWJ significantly enhances jet penetration capability and material removal efficiency while avoiding thermal damage and surface deformation, making it ideal for processing complex materials (e.g., composites, titanium alloys, ceramics). However, challenges persist, including severe nozzle wear, high energy consumption, and substantial capital investment, particularly in high-precision machining of brittle materials like ceramics, where surface roughness control, material removal modeling, and process parameter optimization remain critical yet unresolved issues.

While AWJ technology has achieved notable progress in metal and composite machining, key bottlenecks remain in the efficient precision milling of high-hardness brittle ceramics such as alumina. First, the strong nonlinear coupling between brittle material removal mechanisms and process parameters cannot be adequately captured by traditional single-factor experiments. Second, surface integrity control and depth prediction in ceramic machining lack reliable models, as existing studies predominantly rely on empirical formulas with limited generalizability. Third, systematic process databases for AWJ milling of alumina ceramics remain underdeveloped, hindering industrial adoption. To address these challenges, this study focuses on alumina ceramic plates and employs a hybrid experimental-machine learning approach to overcome these limitations.

This study systematically investigates the AWJ milling process for alumina ceramics, with the following key innovations:

- By integrating single-factor and orthogonal array experiments, the dynamic influence hierarchy of five critical parameters (water jet pressure, abrasive flow rate, nozzle traverse speed, standoff distance, and lateral feed) on material removal rate (MRR) and milling depth is elucidated. For instance, the parameter hierarchy for MRR is identified as water jet pressure > abrasive flow > nozzle speed > standoff distance > lateral feed, transcending the constraints of conventional single-parameter optimization.
- An optimal parameter combination (water jet pressure: 260 MPa, abrasive flow: 240 g/min, standoff distance: 20 mm, etc.) is proposed for brittle alumina ceramics, demonstrating the feasibility of AWJ in precision ceramic machining and filling a critical gap in applied research.
- A nonlinear prediction model for milling depth is innovatively developed using a Radial Basis Function (RBF) neural network. Compared to traditional Backpropagation (BP) networks, the RBF model exhibits superior generalization capabilities on small datasets, achieving a maximum relative error of 17 % and a mean absolute error of 12.01 %, thereby advancing intelligent process optimization tools.
- This work establishes an integrated research framework of "experimental data acquisition → parameter optimization → RBF modeling → process validation" for AWJ milling of alumina ceramics. By synergizing experimental insights with artificial intelligence, it explores the influence mechanisms of multi-parameter interactions on machining performance and delivers a neural network-based depth prediction model. The outcomes provide theoretical foundations and technical solutions for efficient precision machining of ceramics, accelerating the evolution of AWJ technology toward intelligent and high-precision applications.

2. Related work

Abrasive Water Jet Machining has been extensively studied for its capability in precision processing diverse materials. In foundational machinability research, Alberdi *et al.* redefined the separation velocity criterion by evaluating the machinability index, revealing significantly higher Nm values for carbon fiber composites than metals with notable variations between composites [1]. Concurrently, Uthayakumar *et al.* identified water jet pressure as the most critical factor affecting surface morphology in nickel-based superalloys [2]. Regarding key process parameters, Khan and Haque demonstrated that abrasive hardness dictates kerf width and taper during glass machining [3], while Azmir and Ahsan's Taguchi analysis showed water pressure as the dominant factor for surface roughness and abrasive type for taper ratio in glass/epoxy composites [4]. Supriya and Srinivas emphasized that high water pressure and abrasive flow rate enhance cut depth and surface finish in stainless steel [5], and Begic-Hajdarevic *et al.* optimized parameter sets for aluminum balancing productivity and surface quality [6].

For quality prediction and improvement, Hlaváč *et al.* established a theoretical model linking striation deflection angle (θ) to predict maximum cutting speed, with head tilting improving wall quality [7]. Chen and Siores attributed striations to wavelike kinetic energy distribution of abrasives and developed an oscillation technique to increase smooth-zone depth by 30-40 % [8]. Chen *et al.* further applied forward head oscillation in ceramic cutting, noting 70-75 ° impact

angles eliminated trailing striations [9]. Yuvaraj and Kumar corroborated that a 70 ° jet angle better preserved surface integrity in AISI D2 steel versus conventional 90 ° [10].

Studies on specialty materials include research in which Perec identified olivine and crushed glass as cost-effective alternatives to garnet for titanium cutting [11], Niranjan *et al*. validated the applicability of abrasive waterjet machining for AZ91 magnesium alloy [12], Kong *et al*. demonstrated deep milling of NiTi shape-memory alloys [13], Hocheng and Chang derived a 2.5-power relationship between ceramic material removal rate and abrasive velocity, showing that fine abrasives combined with high pressure yield grinding-like surface finishes [14], and Zhu *et al*. achieved ductile-mode polishing of hard-brittle materials to nanoscale surface roughness under low pressure and shallow erosion angles [15].

Cost control strategies were advanced by Kantha Babu and Krishnaiah Chetty, who optimized garnet recycling for aluminum by removing sub-90 μm particles and replenishing at 60 % [16]. Emerging technologies encompass eco-friendly ice jet machining proposed by Gupta *et al.* [17], the optimization of gelatin-bound abrasive water suspension jet (AWSJM) machining by Patel and Tandon [18], Akkurt's geometric characterization of brass cutting fronts [19], Selvan and Raju's analysis of cast iron cutting under varying traverse speeds and standoff distances [20], and solutions for precision cutting of stainless and hardened steels with thicknesses exceeding 10 mm proposed by Hlaváč *et al.* [21].

Radial basis function (RBF) neural networks continue to evolve and demonstrate broad applicability across diverse domains. Notable advances include the Generalized Growing and Pruning RBF (GGAP-RBF) proposed by Huang *et al*., which introduces neuron significance to enable efficient structural adaptation and improved function approximation over existing sequential learning methods [22], and the multi-label RBF (ML-RBF) developed by Zhang, which employs per-class clustering and global weight optimization to capture label correlations, achieving higher accuracy and training speeds exceeding those of BP-MLL by more than two orders of magnitude [23].

Recent advancements in intelligent algorithms have demonstrated potent capabilities in modeling and optimizing complex engineering problems, extending far beyond the realm of AWJ technology. In the fields of localization and transportation, Li *et al.* proposed a UWB-INS fusion positioning approach based on an extended Kalman filter and a two-level error compensation model to improve localization accuracy in GNSS-denied environments. By combining inertial navigation data with UWB measurements and applying wavelet-based prefiltering, their method significantly enhanced positioning accuracy and stability, particularly during changes in vehicle motion states [24]. Leon-Medina *et al.* introduced a bio-inspired topology optimization approach based on bacterial chemotaxis to minimize structural compliance in non-derivative search spaces. The method demonstrated mesh-independent solutions and performance comparable to established evolutionary optimization techniques [25]. Yang *et al.* integrated the Sparrow Search Algorithm (SSA) with Backpropagation Neural Networks (BP), leveraging SSA's global search capability to optimize the BP network. This SSA-BP approach was successfully applied to cloud-based vehicle driving behavior recognition, achieving low identification error, a driving-behavior-based fuel consumption evaluation model with 89.216 % prior accuracy, and approximately 98 % regression fit, offering novel insights for intelligent driving and traffic safety management [26]. Shweta *et al.* developed a low-cost IoT-based monitoring framework for solar photovoltaic power plants using Sigfox LPWAN communication and sensor data analytics, combined with feature selection and deep learning techniques to detect faults and estimate potential energy and energy losses [27]. Lv *et al.* employed Reinforcement Learning to address the Flexible Job-shop Scheduling Problem with Parallel Operations, which captures the synchronization of multiple preceding operations in real manufacturing systems. Their approach is based on an Attention Restart mechanism integrated with Heterogeneous Graph Attention Networks to model complex relationships between operations and machines [28]. Song and Huo investigated manufacturing quality control using ultrasonic nondestructive testing data by integrating machine learning techniques, specifically a wavelet neural network optimized with genetic algorithms. Their approach improved defect prediction accuracy and quality stability evaluation compared to traditional wavelet neural network models, particularly in noisy and complex production environments [29].

In algorithm enhancement and cross-domain application, Chang proposed a revised Girvan-Newman clustering algorithm based on Item Response Theory (IRT) for forming cooperative groups in programming learning. By calculating learner ability and interpersonal relationship metrics, this method significantly improved learning outcomes in programming courses [30]. Zou *et al.* focused on architectural image processing, introducing a novel model integrating Restricted Boltzmann Machines (RBMs) and Convolutional Neural Networks (CNNs). This model achieved high-accuracy (97 %) and efficient 2D-to-3D conversion of architectural images, substantially improving measurement precision and reducing execution time [31]. These interdisciplinary studies underscore the significant potential of intelligent algorithms (e.g., NN, SVM, GA, PSO variants, DRL, GP) in modeling complex systems, optimizing parameters, and enhancing performance. Their successful methodologies and findings offer valuable insights and synergistic possibilities for the intelligent advancement of AWJ technology, particularly in areas like parameter optimization, quality prediction, and process control.

3. Research method

3.1 Experimental setup and materials

The experiment employed a five-axis ultra-high-pressure abrasive water jet system, which primarily consists of a high-pressure generator, water softening system, abrasive feeding system, control system, and nozzle assembly. The schematic diagram of this cutting experimental setup is shown in Fig. 1.

The milling workpiece material was YHL02 alumina ceramic plate, as shown in Fig. 2. The performance parameters of the alumina ceramic material are listed in Table 1.

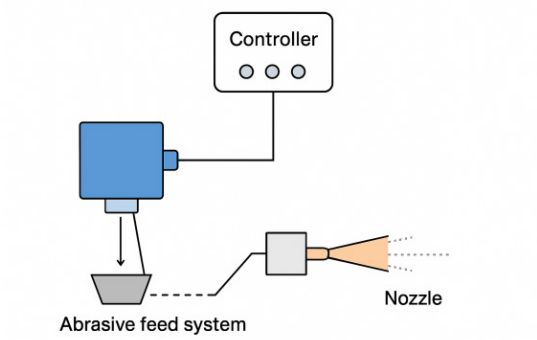

Fig. 1 High pressure generating system

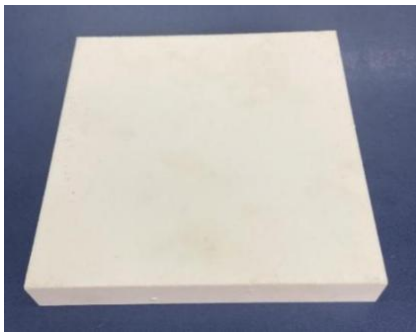

Fig. 2 Alumina ceramic plate sample

Table 1 Mechanical properties of workpiece

Experimental material	Content (%)	Vickers hardness (GPa)	Compressive strength (MPa)	Fracture toughness (MPa·m$^{1/2}$)	Density (g/cm^3)	Modulus of elasticity (GPa)
Al2O3	92	10.4	850	4.8	3.2	276

3.2 Experimental design for milling

The experimental procedure involved milling a groove (30 × 10 × 2 mm^3) in the alumina ceramic workpiece. Fig. 3 shows the programmed nozzle trajectory, using conventional 60-mesh garnet abrasive.

Considering experimental constraints, five dominant and controllable process parameters were investigated: jet pressure (MPa), nozzle traverse speed (mm/min), standoff distance (mm), stepover (mm), and abrasive mass flow rate (g/min). The parameter matrix for alumina ceramic milling is presented in Table 2.

The experimental setup includes (Fig. 4):

- workpiece fixturing arrangement,
- in-process milling demonstration.

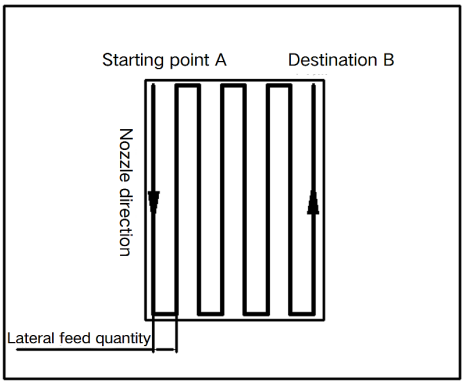

Fig. 3 The milling path

Table 2 Process parameters for milling alumina ceramics

Process parameter	Parameter level								
Jet pressure P (MPa)	220	230	240	250	260	270	280	290	300
Target range S (mm)	5	7	10	13	15	17	20	23	25
Nozzle velocity u (mm/min)	50	75	100	125	150	175	200	225	250
Lateral feed L (mm)	0.6	0.65	0.7	0.75	0.8	0.85	0.9	0.95	1.0
Abrasive flow m_a (g/min)	60	90	120	150	180	210	240	270	300

(a) (b)

Fig. 4 The milling experiment

The machining performance of abrasive water jet milling is evaluated by two key indicators: material volume removal rate and single-pass cutting depth. The average material removal rate (V) is calculated by dividing the total removed material volume by the milling time. The material removal volume, representing the volumetric amount removed in a single milling pass, can be determined by dividing the removed material mass by its density. The milling time is obtained through empirical formulas Eq. 1 [32].

$$T = \frac{bl}{\delta u} N_a \tag{1}$$

where T is milling time (s), l is length of milling plane (mm), δ is single-pass milling width (mm), u is nozzle traverse speed (mm/s), b is width of milling plane (mm), and N_a is number of milling passes. The depth of milling (h) was determined by averaging three caliper measurements.

3.3 The establishment of RBF

Radial basis function neural networks (RBFNNs) are well suited for predicting abrasive water jet milling depth due to their strong nonlinear mapping capability and efficient learning characteristics, particularly for small data sets. Its applicability is primarily demonstrated in abrasive water jet machining, where complex nonlinear coupling relationships exist between milling depth and process parameters such as jet pressure (P), nozzle moving speed (u), and others. The RBFNN locally transforms the input space using Gaussian functions in the hidden layer, enabling effective capture of nonlinear interactions between parameters and overcoming the limitations of traditional linear methods, such as polynomial regression. Moreover, given the limited amo-

unt of experimental data (45 data sets) and the dynamic neuron expansion mechanism implemented in the hidden layer of the RBFNN via the MATLAB *newrb* function, overfitting can be avoided by gradually increasing the number of neurons according to a predefined target error. Compared with the BP neural network, the RBFNN exhibits stronger generalization ability when applied to small data sets.

Experimental data source

The experimental system comprises 45 data sets obtained from single-factor abrasive water jet milling tests, covering the following parameter ranges: jet pressure P (220-300 MPa), nozzle moving speed u (50-250 mm/min), target distance S (5-25 mm), lateral feed L (0.6-1.0 mm), and abrasive flow rate m_a 60-300 g/min.

Data preprocessing

Min–Max normalization was applied using Eq. 2:

$$x_{norm} = \frac{x - x_{min}}{x_{max} - x_{min}} \tag{2}$$

To avoid data leakage, the normalization parameters derived from the training set were also applied to the test set. After normalization, all variables were scaled to the interval [0,1], which effectively improves the convergence speed of the network.

Validation data set

To verify the predictive capability of the model, nine validation experiments were conducted using different combinations of five process parameters. The corresponding measured milling depths are summarized in Table 3.

Table 3 Validation experimental data set for milling depth prediction

Argument / Serial number	P (MP)	S (mm)	u (mm/min)	L (mm)	m_a (g/min)	Actual milling depth
1	220	6	61.82	0.6	80	0.88
2	230	8	71.66	0.7	100	0.65
3	250	11	89.46	0.8	130	0.53
4	270	12	100.50	0.9	150	0.71
5	290	17	127.17	0.65	200	1.25
6	295	22	174.58	0.75	250	1.64
7	200	7	98.10	0.4	70	1.59
8	205	13	108.67	0.5	90	1.01
9	225	5	200	1.0	110	1.42

A Radial Basis Function Neural Network (RBFNN) adopts a three-layer feed forward structure, and its topological design strictly follows theoretical framework proposed by Broomhead and Lowe [33]. According to the five-dimensional input characteristics of abrasive water jet processing (jet pressure P, nozzle moving speed u, target distance S, lateral feed rate L, and abrasive flow rate m_a), the network is constructed as follows:

- Input layer: Five neurons corresponding to the standardized process parameter vector $X = [P, u, S, L, m_a]^{\mathrm{T}}$
- Hidden layer: The number of neurons is determined adaptively and generated iteratively using the MATLAB *newrb* function.
- Output layer: One linear neuron that outputs the predicted milling depth.

Among them, the activation function of the j-th neuron in the hidden layer is defined as a Gaussian radial basis function, as shown in Eq. (3):

$$\phi_j(x) = \exp\left(-\frac{\|x - c_j\|^2}{2\sigma_j^2}\right) \tag{3}$$

where c_j is the center of the j-th basis function, σ_j is the width parameter, and $||\cdot||$ denotes the Euclidean norm.

Key parameter optimization

The optimal parameter combination determined by grid search is shown in Table 4.

Table 4 Optimal parameter combination

Spread	1.0
Goal	0.001
Maximum number of neurons	45

For the performance evaluation of the model, the root mean square error (RMSE) and the coefficient of determination R^2 are employed. The root mean square error is defined in Eq. (4):

$$RMSE = \sqrt{\frac{1}{n}\sum_{i=1}^{n}(y_i - \hat{y}_i)^2} \tag{4}$$

The coefficient of determination is defined in Eq. (5):

$$R^2 = 1 - \frac{\sum_{i=1}^{n}(y_i - \hat{y}_i)^2}{\sum_{i=1}^{n}(y_i - \bar{y})^2} \tag{5}$$

4. Results

4.1 Results of single milling experiment

The influence of injection pressure

During the experiment, the nozzle moving speed was 50 mm/min, the target distance was 10 mm, the lateral feed rate was 0.6 mm, and the abrasive flow rate was 120 g/min. The jet pressure varied from 220 to 300 MPa in increments of 10 MPa. Fig. 5 shows the effect of jet pressure P on the material removal rate and the average milling depth of alumina ceramics.

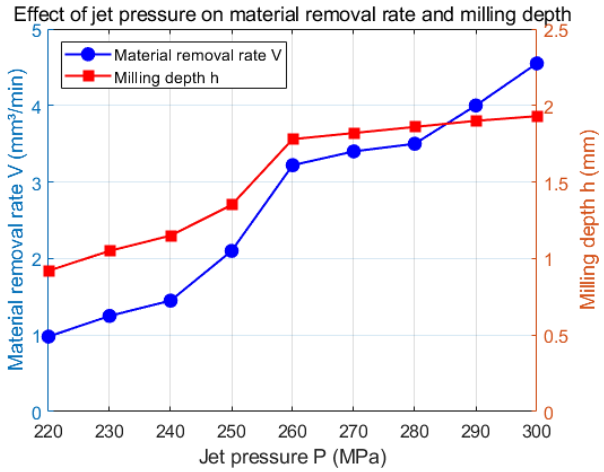

Fig. 5 Effect of the jet pressure P on the volume removal rate V and milling depth h of alumina ceramics

As can be seen from the figure, with the increase of jet pressure P, the material removal rate V presents nearly linear increase trend, and the jet pressure P is positively correlated with the material removal rate V, because the jet energy increases with the increase of jet pressure P, while the material removal rate V depends on the energy exerted on the workpiece surface per unit time. When removing materials, it is easier to reach the stress of material shedding, so the material removal rate is positively correlated with it.

The influence of the nozzle's moving speed

During the experiment, the jet pressure is 260 MPa, the target distance was 10 mm, the lateral feed rate was 0.6 mm, and the abrasive flow rate was 120 g/min. The nozzle moving speed was

varied from 50 to 250 mm/min in increments of 25 mm/min. Fig. 6 shows the effect of the nozzle moving speed u on the material removal rate and the average milling depth of alumina ceramics.

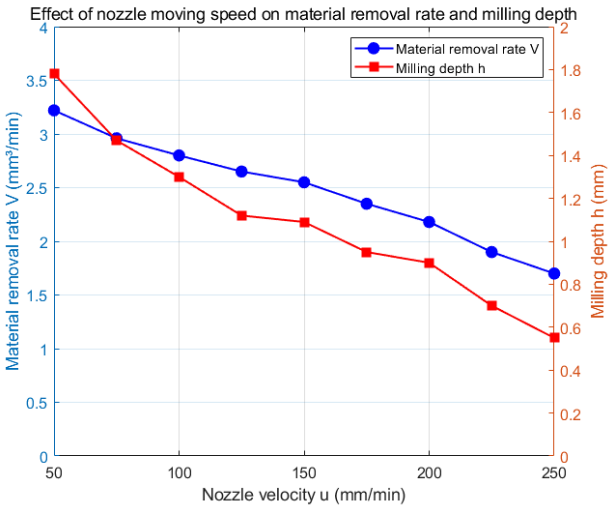

Fig. 6 Influence of the nozzle moving speed u on the volume removal rate V and milling depth h of alumina ceramics

As can be seen from the figure, as the nozzle moving speed u increases, the material removal rate V gradually decreases. This is because, at lower nozzle moving speeds, the interaction time between the jet and the workpiece material is longer, which facilitates material removal but reduces processing efficiency. Conversely, as the milling speed increases, the average impact energy of the jet acting on the workpiece decreases, resulting in a lower material removal rate.

The influence of the target distance

When the jet pressure was 260 MPa, the nozzle moving speed was 50 mm/min, the lateral feed rate was 0.6 mm, and the abrasive flow rate was 120 g/min, the target distance was varied from 5 to 25 mm (5, 7, 10, 13, 15, 17, 20, 23, and 25 mm). Fig. 7 shows the effect of the target distance S on the average material removal rate and milling depth of alumina ceramics.

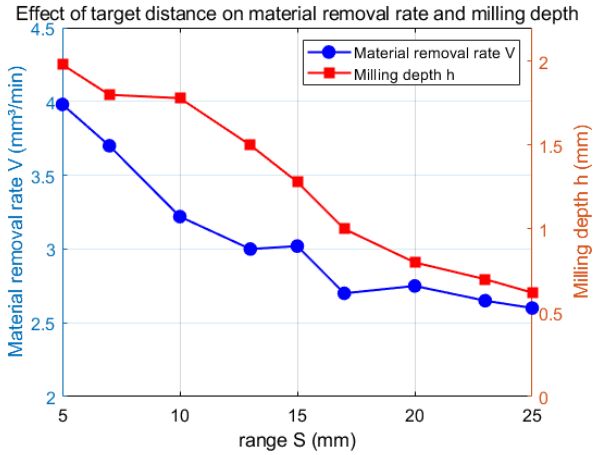

Fig. 7 Influence of the target distance S on the volume removal rate V and milling depth h of alumina ceramics

As can be seen from the figure, with the increase of target distance S, the material removal rate V decreases. This is because, with increasing target distance, the jet is increasingly affected by diffusion and air resistance, causing it to reach the workpiece surface in a more divergent form. As a result, the effective milling area increases, while the number of abrasive particles impacting the workpiece per unit area decreases, leading to a reduction in the kinetic energy transferred during impact. Consequently, the material stripping capability is weakened, resulting in a lower material removal rate.

The influence of lateral feed rate

The milling process usually requires multiple cuts to achieve the desired groove dimensions, and the lateral feed indicates the distance between the centers of adjacent abrasive water jets. According to the experimental data in Table 2, the jet pressure was 260 MPa, the nozzle moving speed was 50 mm/min, the target distance was 10 mm, and the abrasive flow rate was 120 g/min. The transverse feed rate L was varied from 0.6 to 1.0 mm (0.6, 0.65, 0.7, 0.75, 0.8, 0.85, 0.9, 0.95, and 1.0 mm). Fig. 8 shows the effect of the transverse feed rate L on the material removal rate and the average milling depth of alumina ceramics.

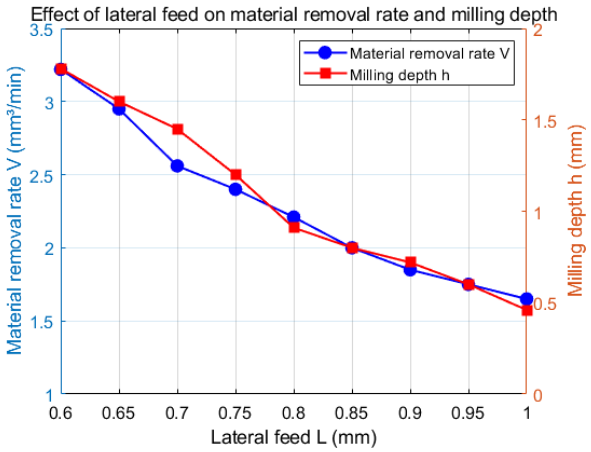

Fig. 8 Effect of the lateral feed L on the volume removal rate V and milling depth h of alumina ceramics

As can be seen from the figure, the material removal rate of alumina ceramics decreases with increasing lateral feed rate. This is because, as the transverse feed rate increases, the overlap area between adjacent cuts decreases, resulting in portions of material remaining unprocessed between neighboring tracks and, consequently, a lower material removal rate. However, when the lateral feed rate is too small, the material stripping efficiency is reduced and the milling depth becomes excessively large due to repeated milling. Therefore, an appropriate lateral feed rate should be selected.

The influence of abrasive flow rate

When the jet pressure was 260 MPa, the nozzle moving speed was 50 mm/min, the lateral feed rate was 0.6 mm, and the target distance was 10 mm, the abrasive flow rate was varied from 60 to 300 g/min (60, 90, 120, 150, 180, 210, 240, 270, and 300 g/min). Fig. 9 shows the effect of the abrasive flow rate on the volume removal rate and the average milling depth of alumina ceramics.

As can be seen from the figure, the material removal rate increases with increasing abrasive flow rate. This is because, as the abrasive flow rate increases, the number of abrasive particles per unit volume of the jet also increases, leading to a higher number of particles participating in the erosion process. Consequently, the frequency of abrasive impacts on the workpiece surface increases. Since material removal is primarily governed by abrasive particle erosion, a higher abrasive flow rate results in an increased material removal rate.

Based on the above single-factor experimental results, an optimal parameter combination was identified. Under the optimal conditions (jet pressure of 260 MPa, abrasive flow rate of 240 g/min, and nozzle moving speed of 50 mm/min), a surface roughness Ra of 3.2 μm was achieved, representing a reduction of 28 % compared with the baseline condition. This improvement also led to an estimated reduction of post-processing time by approximately 20 %.

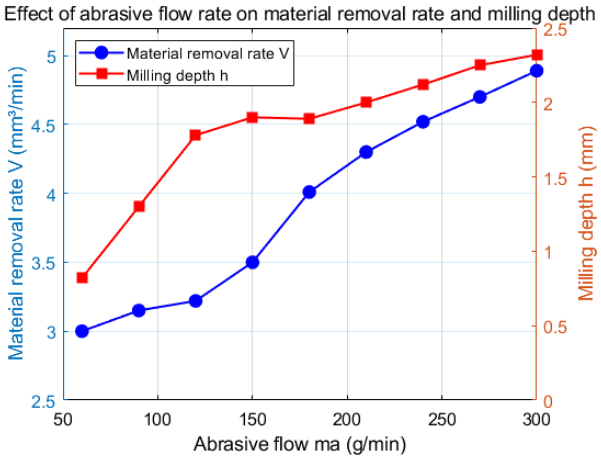

Fig. 9 Effect of the abrasive flow rate m_a on the volume removal rate V and milling depth h of alumina ceramics

4.2 Results of orthogonal experiment

Several easily controllable parameters, such as jet pressure, nozzle moving speed, and abrasive flow rate, have a significant influence on machining performance when considered individually. However, in actual production and processing, these process parameters must be analyzed comprehensively. Therefore, an orthogonal experimental method is employed to further optimize the five process parameters and identify the optimal combination of machining conditions.

In this experiment, jet pressure P, nozzle moving speed u, lateral feed rate L, target distance S, and abrasive flow rate m_a were selected as the process parameters. Four levels were defined for each factor. Since all factors had the same number of levels, an L16 (4^5) orthogonal array with five factors and four levels was employed, resulting in a total of 16 experiments. The experimental factors and their corresponding levels are listed in Table 5, while the orthogonal experimental design and results are presented in Table 6.

Table 5 Test factors and levels

Factor level	Jet pressure P(MPa)	Abrasive flow m_a (g/min)	Target Range S(mm)	Lateral feed L (mm)	Nozzle moving speed u (mm/min)
1	240	60	10	0.6	50
2	260	120	15	0.7	100
3	280	180	20	0.8	150
4	300	240	25	0.9	200

Table 6 Orthogonal experiment table and experiment results

Number	Experimental parameter					Experimental result	
	A	B	C	D	E		
	P (MPa)	m_a (g/min)	S (mm)	L (mm)	u (mm/min)	Volume removal rate V (mm³/s)	Milling depth h(mm)
1	240	60	10	0.6	50	1.12	1.25
2	240	120	15	0.7	100	0.78	1.18
3	240	180	20	0.8	150	0.85	1.20
4	240	240	25	0.9	200	0.64	1.14
5	260	60	15	0.8	200	2.05	1.62
6	260	120	10	0.9	150	2.25	1.73
7	260	180	25	0.6	100	3.58	2.15
8	260	240	20	0.7	50	3.89	2.52
9	280	60	20	0.9	100	1.85	1.47
10	280	120	25	0.8	50	2.15	1.58
11	280	180	10	0.7	200	1.96	1.51
12	280	240	15	0.6	150	2.43	1.92
13	300	60	25	0.7	150	1.52	1.50
14	300	120	20	0.6	200	2.78	1.72
15	300	180	15	0.9	50	3.54	1.93
16	300	240	10	0.8	100	4.35	2.18

The optimized parameter ranges identified in this study (e.g., jet pressure of 260-300 MPa and abrasive flow rate of up to 240 g/min) are compatible with commercially available five-axis abrasive water jet systems. Furthermore, an industrial case study conducted at a ceramics manufacturing facility in Sichuan, China, demonstrated that applying the optimized parameters resulted in an approximately 12 % improvement in processing efficiency, indicating good industrial scalability of the proposed optimization strategy.

4.3 RBF prediction results

By running the RBF prediction code in MATLAB, as shown in Fig. 10, nine independent test data sets were obtained for model validation, yielding an RMSE of 0.1569 and an R^2 value of 0.8404. The results indicate that the RBF neural network is capable of accurately fitting the abrasive water jet milling depth, with an average absolute error of 12.01 %. The maximum absolute error occurred in validation sample No. 7 and reached 0.3. The maximum relative error occurred in validation sample No. 2, with a value of 17 %.

For comparison, support vector machine (SVM) and random forest regression (RFR) models were also evaluated using the same data set. The RBF model achieved an RMSE of 0.1569 and an R^2 value of 0.8404, compared with RMSE values of 0.1925 and 0.2013 and R^2 values of 0.7812 and 0.7545 for the SVM and RFR models, respectively, indicating the superior predictive performance of the RBF model.

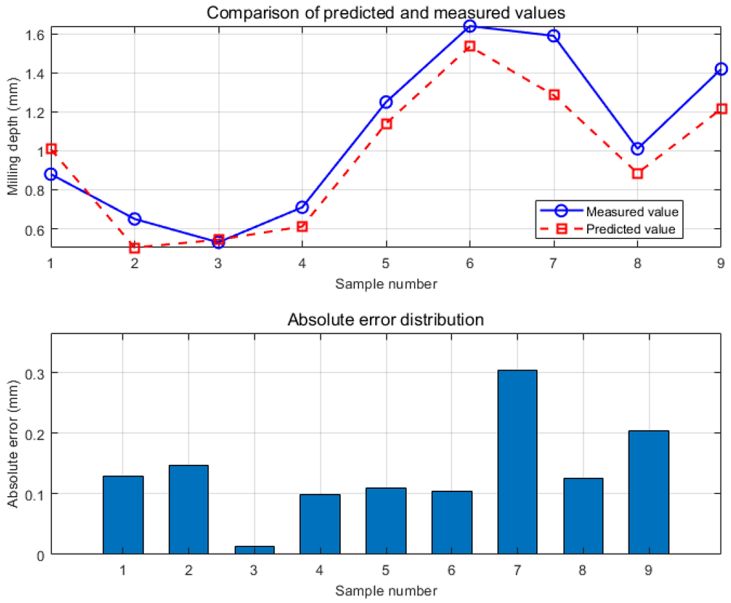

Fig. 10 RBF prediction results and absolute errors

5. Discussion

5.1 Discussion on a single milling experiment

The experimental results reveal systematic relationships between key process parameters and milling depth h during abrasive water jet (AWJ) milling of alumina ceramics. These dependencies are governed by fundamental energy transfer and material removal mechanisms.

Jet pressure P

The milling depth h exhibits a strong positive correlation with the jet pressure P. Increasing P elevates the kinetic energy of the jet, enabling more effective material erosion at greater depths within the workpiece. Higher energy density facilitates overcoming the material's fracture toughness at subsurface layers. However, excessively high P imposes greater demands on the ultra-high-pressure intensifier system and significantly increases energy consumption. Optimal pressure selection is therefore critical to balance machining efficiency with equipment longevity and operational costs.

Nozzle traverse speed u

An inverse relationship exists between traverse speed u and the milling depth h. Higher traverse speeds reduce the dwell time of the jet over any given point on the workpiece, thereby decreasing the total impact energy delivered per unit area per unit time. Consequently, material removal primarily occurs near the surface, with insufficient energy reaching deeper regions to cause effective fracture. The reduced interaction time ultimately limits penetration depth.

Standoff distance S

An increase in the standoff distance S leads to a reduction in the milling depth h. As the jet travels a longer distance through air, aerodynamic drag causes jet dispersion and attenuation of kinetic energy. The expanding jet profile reduces particle density and impact velocity upon reaching the workpiece surface, thereby diminishing its ability to erode material effectively at greater depths. Notably, beyond a critical standoff distance (approximately 20 mm in this study), jet energy dissipation reaches a level at which further increases in S result in negligible changes in both the material removal rate V and the milling depth h. This behavior indicates that the jet enters a regime where its residual energy falls below the threshold required for significant material removal in the hard alumina substrate.

Lateral feed L

The milling depth h is inversely related to the lateral feed L. A smaller L increases the overlap between successive jet passes, subjecting the material within the overlap zone to repeated impacts and thereby increasing the cumulative erosion depth in these regions. In contrast, a larger L reduces the overlap between adjacent passes, leaving valleys of unprocessed or minimally processed material between milled tracks, which ultimately leads to a reduction in the overall milling depth across the machined area.

Abrasive mass flow rate m_a

The milling depth h increases with increasing abrasive mass flow rate m_a. A higher abrasive flow rate introduces a greater number of abrasive particles into the jet stream per unit time, which increases the frequency of particle impacts on the workpiece surface and subsurface per unit area. The cumulative kinetic energy transferred by the increased particle flux generates higher normal and shear stresses within the material, enabling the fracture threshold to be exceeded over a larger volume. As a result, deeper penetration and enhanced material removal are achieved.

Overall, the observed dependencies indicate that the milling depth h is predominantly governed by the effective kinetic energy density delivered to the workpiece subsurface. Parameters such as jet pressure P and abrasive mass flow rate m_a directly increase this energy density, thereby promoting deeper erosion. In contrast, nozzle traverse speed u, standoff distance S, and lateral feed L act to reduce or redistribute the delivered energy density—u by limiting exposure time, S by dissipating energy prior to impact, and L by spatially distributing the energy input across the machined area. The identified saturation behavior with respect to S highlights the importance of maintaining an optimal standoff distance to maximize jet efficiency. These findings provide a clear mechanistic basis for the parameter optimization achieved through orthogonal experiments and support the physical validity of the predictive relationships captured by the RBF neural network model.

From an industrial perspective, high-energy process parameters increase operational costs. Operating at 300 MPa consumes approximately 0.22 kWh per minute, adding about 0.03-0.04 USD per minute and reducing nozzle service life by 18-22 % compared with 250 MPa. Abrasive consumption dominates the total cost (65-75 %), followed by energy (15-20 %) and nozzle wear (8-10 %), indicating the importance of balancing performance and cost efficiency.

Nozzle wear under high-pressure conditions can be mitigated through appropriate material selection. Tungsten carbide nozzles extend service life by about 40 %, diamond-lined nozzles reduce wear by up to 60 %, and coarser abrasives (e.g., 80 mesh) lower impact stress by approximately 20 %, improving nozzle durability.

5.2 Discussion on orthogonal experiment results

For the analysis of orthogonal experimental data, the range analysis method is employed to evaluate the relative influence of each process parameter, as defined in Eq. 6:

$$R = \max(T_1, T_2, T_3, T_4) - \min(T_1, T_2, T_3, T_4) \quad (6)$$

Based on the results presented in Table 7, the influence of the experimental factors on the material removal rate can be ranked as follows: jet pressure P > abrasive flow rate m_a > nozzle traverse speed u > standoff distance S > lateral feed L. The optimal parameter combination for maximizing the material removal rate is identified as $A_4B_4C_1D_1E_1$, corresponding to a jet pressure of 300 MPa, an abrasive flow rate of 240 g/min, a standoff distance of 10 mm, a lateral feed rate of 0.6 mm, and a nozzle traverse speed of 50 mm/min.

Similarly, according to the range analysis results in Table 8, the influence of the experimental factors on milling depth can be ordered as follows: jet pressure P > abrasive flow rate m_a > nozzle traverse speed u > lateral feed L > standoff distance S. The optimal parameter combination for maximizing the milling depth is $A_2B_4C_3D_1E_1$, corresponding to a jet pressure of 260 MPa, an abrasive flow rate of 240 g/min, a standoff distance of 20 mm, a lateral feed rate of 0.6 mm, and a nozzle traverse speed of 50 mm/min.

From a practical manufacturing standpoint, operating at high jet pressures increases process costs. Operating at a pressure of 300 MPa requires a power input of approximately 13.2 kW, adds about 0.03-0.04 USD per minute, and reduces nozzle life by 18-22 % compared with 250 MPa. Abrasives account for 65-75 % of total costs, followed by energy (15-20 %) and nozzle wear (8-10 %), emphasizing the need to balance performance and cost efficiency.

Table 7 Range analysis of experimental results for the material removal rate V in abrasive water jet single-pass milling

Factor / Index	A	B	C	D	E
	P (MPa)	m_a (g/min)	S (mm)	L (mm)	u (mm/min)
T1	3.39	6.54	9.68	9.91	10.70
T2	11.77	7.96	8.80	8.15	10.56
T3	8.39	9.93	9.37	9.40	7.05
T4	12.19	11.31	7.89	8.28	7.43

Table 8 Range analysis of experimental results for single-pass milling depth h in abrasive water jet machining

Factor / Index	A	B	C	D	E
	P (MPa)	m_a (g/min)	S (mm)	L (mm)	u (mm/min)
T1	0.77	1.84	2.63	3.04	3.28
T2	4.02	2.21	2.65	2.71	2.98
T3	2.48	2.79	2.91	2.58	2.35
T4	3.33	3.76	2.37	2.27	1.99

5.3 Discussion on RBF prediction

With jet pressure, nozzle moving speed, target distance, lateral feed rate, and abrasive particle size serving as the inputs of the RBF neural network, and milling depth as the output, the optimal parameter combination was determined using a grid search algorithm. Based on the experimental data, an RBF neural network model for predicting milling depth was established, yielding predicted milling depth values. The maximum absolute error compared with the measured milling depth is 0.3 mm, while the maximum relative error is 17 %. Furthermore, the milling depth can be effectively controlled by adjusting the jet pressure, nozzle moving speed, target distance, lateral feed rate, and abrasive particle size.

In industrial applications, accurate prediction of milling depth is particularly important under high-pressure operating conditions. Operating at a jet pressure of 300 MPa requires a power consumption of approximately 13.2 kW and reduces nozzle service life by 18-22 % compared with 250 MPa. Therefore, reliable RBF-based prediction can assist in selecting appropriate process parameters to reduce unnecessary energy consumption and tool wear while maintaining machining performance.

6. Conclusion

Through an experimental study of abrasive water jet milling of alumina ceramic sheets, the following conclusions are drawn:

- Systematic single-factor and orthogonal experiments revealed the influence hierarchy of five key parameters (jet pressure P, nozzle speed u, standoff distance S, transverse feed L, and abrasive flow rate m_a) on machining performance. For the material removal rate V, the dominant parameters followed the order $P > m_a > u > S > L$, with optimal settings of P = 300 MPa, m_a = 240 g/min, S = 10 mm, L = 0.6 mm, and u = 50 mm/min. For the milling depth h, the hierarchy shifted to $P > m_a > u > L > S$, with optimal parameters of P = 260 MPa, m_a = 240 g/min, S = 20 mm, L = 0.6 mm, and u = 50 mm/min.
- A radial basis function neural network (RBFNN) model implemented in MATLAB demonstrated reliable predictive capability for milling depth under multi-parameter conditions. Validation using nine independent experimental cases yielded a maximum relative error of 17 % (corresponding to a maximum absolute error of 0.3 mm) and a mean absolute error of 12.01 %, confirming the feasibility and effectiveness of neural-network-based modeling for nonlinear abrasive water jet machining processes.

References

[1] Alberdi, A., Suárez, A., Artaza, T., Escobar-Palafox, G.A., Ridgway, K. (2013). Composite cutting with abrasive water jet, *Procedia Engineering*, Vol. 63, 421-429, doi: 10.1016/j.proeng.2013.08.217.

[2] Uthayakumar, M., Khan, M.A., Kumaran, S.T., Slota, A., Zajac, J. (2016). Machinability of nickel-based superalloy by abrasive water jet machining, *Materials and Manufacturing Processes*, Vol. 31, No. 13, 1733-1739, doi: 10.1080/10426914.2015.1103859.

[3] Khan, A.A., Haque, M.M. (2007). Performance of different abrasive materials during abrasive water jet machining of glass, *Journal of Materials Processing Technology*, Vol. 191, No. 1-3, 404-407, doi: 10.1016/j.jmatprotec.2007.03.071.

[4] Azmir, M.A., Ahsan, A.K. (2009). A study of abrasive water jet machining process on glass/epoxy composite laminate, *Journal of Materials Processing Technology*, Vol. 209, No. 20, 6168-6173, doi: 10.1016/j.jmatprotec.2009.08.011.

[5] Supriya, S.B., Srinivas, S. (2018). Machinability studies on stainless steel by abrasive water jet – Review, *Materials Today: Proceedings*, Vol. 5, No. 1, Part 3, 2871-2876, doi: 10.1016/j.matpr.2018.01.079.

[6] Begic-Hajdarevic, D., Cekic, A., Mehmedovic, M., Djelmic, A. (2015). Experimental study on surface roughness in abrasive water jet cutting, *Procedia Engineering*, Vol. 100, 394-399, doi: 10.1016/j.proeng.2015.01.383.

[7] Hlaváč, L.M., Hlaváčová, I.M., Gembalová, L., Kaličinský, J., Fabian, S., Měšťánek, J., Kmec, J., Mádr, V. (2009). Experimental method for the investigation of the abrasive water jet cutting quality, *Journal of Materials Processing Technology*, Vol. 209, No. 20, 6190-6195, doi: 10.1016/j.jmatprotec.2009.04.011.

[8] Chen, F.L., Siores, E. (2001). The effect of cutting jet variation on striation formation in abrasive water jet cutting, *International Journal of Machine Tools and Manufacture*, Vol. 41, No. 10, 1479-1486, doi: 10.1016/S0890-6955(01)00013-X.

[9] Chen, L., Siores, E., Wong, W.C.K. (1998). Optimising abrasive waterjet cutting of ceramic materials, *Journal of Materials Processing Technology*, Vol. 74, No. 1-3, 251-254, doi: 10.1016/S0924-0136(97)00278-1.

[10] Yuvaraj, N., Kumar, M.P. (2016). Surface integrity studies on abrasive water jet cutting of AISI D2 steel, *Materials and Manufacturing Processes*, Vol. 32, No. 2, 162-170, doi: 10.1080/10426914.2016.1221093.

[11] Perec, A. (2018). Experimental research into alternative abrasive material for the abrasive water-jet cutting of titanium, *The International Journal of Advanced Manufacturing Technology*, Vol. 97, 1529-1540, doi: 10.1007/s00170-018-1957-2.

[12] Niranjan, C.A., Srinivas, S., Ramachandra, M. (2018). Effect of process parameters on depth of penetration and topography of AZ91 magnesium alloy in abrasive water jet cutting, *Journal of Magnesium and Alloys*, Vol. 6, No. 4, 366-374, doi: 10.1016/j.jma.2018.07.001.

[13] Kong, M.C., Axinte, D., Voice, W. (2011). Challenges in using waterjet machining of NiTi shape memory alloys: an analysis of controlled-depth milling, *Journal of Materials Processing Technology*, Vol. 211, No. 6, 959-971, doi: 10.1016/j.jmatprotec.2010.12.015.

[14] Hocheng, H., Chang, K.R. (1994). Material removal analysis in abrasive waterjet cutting of ceramic plates, *Journal of Materials Processing Technology*, Vol. 40, No. 3-4, 287-304, doi: 10.1016/0924-0136(94)90456-1.

[15] Zhu, H.T., Huang, C.Z., Wang, J., Li, Q.L., Che, C.L. (2009). Experimental study on abrasive waterjet polishing for hard-brittle materials, *International Journal of Machine Tools and Manufacture*, Vol. 49, No. 7-8, 569-578, doi: 10.1016/j.ijmachtools.2009.02.005.

[16] Kantha Babu, M., Krishnaiah Chetty, O.V. (2002). Studies on recharging of abrasives in abrasive water jet machining, *The International Journal of Advanced Manufacturing Technology*, Vol. 19, 697-703, doi: 10.1007/s001700200115.
[17] Gupta, K., Avvari, M., Mashamba, A., Mallaiah, M. (2017). Ice jet machining: A sustainable variant of abrasive water jet machining, In: Davim, J. (eds.), *Sustainable Machining*, Springer, Cham, Switzerland, 67-78, doi: 10.1007/978-3-319-51961-6_4.
[18] Patel, D., Tandon, P. (2017). Experimental investigations of gelatin-enabled abrasive water slurry jet machining, *The International Journal of Advanced Manufacturing Technology*, Vol. 89, 1193-1208, doi: 10.1007/s00170-016-9154-7.
[19] Akkurt, A. (2010). Cut front geometry characterization in cutting applications of brass with abrasive water jet, *Journal of Materials Engineering and Performance*, Vol. 19, 599-606, doi: 10.1007/s11665-009-9513-8.
[20] Selvan, M.C.P., Raju, N.M.S. (2012). Analysis of surface roughness in abrasive waterjet cutting of cast iron, *International Journal of Science, Environment and Technology*, Vol. 1, No. 3, 174-182.
[21] Hlaváč, L.M., Hlaváčová, I.M., Geryk, V., Plančár, Š. (2015). Investigation of the taper of kerfs cut in steels by AWJ, *The International Journal of Advanced Manufacturing Technology*, Vol. 77, 1811-1818, doi: 10.1007/s00170-014-6578-9.
[22] Huang, G.-B., Saratchandran, P., Sundararajan, N. (2005). A generalized growing and pruning RBF (GGAP-RBF) neural network for function approximation, *IEEE Transactions on Neural Networks*, Vol. 16, No. 1, 57-67, doi: 10.1109/TNN.2004.836241.
[23] Zhang, M.-L. (2009). ML-RBF: RBF neural networks for multi-label learning, *Neural Processing Letters*, Vol. 29, 61-74, doi: 10.1007/s11063-009-9095-3.
[24] Li, Z., Zhang, Y., Shi, Y., Yuan, S., Zhu, S. (2023). Performance enhancement of INS and UWB fusion positioning method based on two-level error model, *Sensors,* Vol. 23, No. 2, Articel No. 557, doi: 10.3390/s23020557.
[25] Leon-Medina, J.X., Giraldo, J.F., Guzmán, M.A., Villalba-Morales, J.D. (2025). A bacterial chemostatic-based bio-inspired algorithm for the structural optimization of planar structures, *Arabian Journal for Science and Engineering*, 1-21, doi: 10.1007/s13369-025-10749-y.
[26] Yang, X., Xiang, K., Yuan, S., Huang, J. (2024). Vehicle driving behavior recognition and optimization strategies based on cloud computing and SSA-BP algorithm, *Studies in Informatics and Control*, Vol. 33, No. 3, 17-28, doi: 10.24846/v33i3y202402.
[27] Shweta, R., Sivagnanam, S., Kumar, K.A. (2023). IoT-based Deep Learning Neural Network (DLNN) algorithm for voltage stability control and monitoring of solar power generation, *Advances in Production Engineering & Management*, Vol. 18, No. 4, 447-461, doi: 10.14743/apem2023.4.484.
[28] Lv, Q.H., Chen, J., Chen, P., Xun, Q.F., Gao, L. (2024). Flexible Job-shop Scheduling Problem with parallel operations using Reinforcement Learning: An approach based on Heterogeneous Graph Attention Networks, *Advances in Production Engineering & Management*, Vol. 19, No. 2, 157-181, doi: 10.14743/apem2024.2.499.
[29] Song, W.T., Huo, L. (2024). Machine learning for enhancing manufacturing quality control in ultrasonic nondestructive testing: A Wavelet Neural Network and Genetic Algorithm approach, *Advances in Production Engineering & Management*, Vol. 19, No. 3, 347-357, doi: 10.14743/apem2024.3.511.
[30] Chang, W.-C. (2024). A revised Girvan-Newman clustering algorithm for cooperative groups detection in programming learning, *Computer Science and Information Systems*, Vol. 21, No. 2, 491-505, doi: 10.2298/CSIS220830069C.
[31] Zou, Q., Liu, F., Liao, Y. (2024). Enhancing architectural image processing: A novel 2D to 3D algorithm using improved convolutional neural networks, *Computer Science and Information Systems*, Vol. 21, No. 4, 1457-1481, doi: 10.2298/CSIS230725043Z.
[32] Feng, Y. (2007). *Research on machining technology of abrasive water jet milling ceramic materials* (in Chinese), PhD thesis, Shandong University, China.
[33] Broomhead, D.S., Lowe, D. (1988). Multivariable functional interpolation and adaptive networks, *Complex Systems*, Vol. 2, 321-355.